energies

MDPI

Article

The Impacts of Nano-Micrometer Pore Structure on the Gas Migration and Accumulation in Tight Sandstone Gas Reservoirs

Juncheng Qiao [1,2,3], Xianzheng Zhao [4], Jianhui Zeng [1,2,*], Guomeng Han [4], Shu Jiang [3,5,*], Sen Feng [1,2] and Xiao Feng [1,2]

1 State Key Laboratory of Petroleum Resources and Prospecting, China University of Petroleum, Beijing 102249, China; 2014311027@student.cup.edu.cn (J.Q.); 2017311025@student.cup.edu.cn (S.F.); 2016311029@student.cup.edu.cn (X.F.)
2 College of Geosciences, China University of Petroleum, Beijing 102249, China
3 Energy & Geosciences Institute and Department of Chemical Engineering, University of Utah, Salt Lake City, UT 84108, USA
4 Dagang oil field company, Petrochina, Tianjin 300280, China; xzzhao@petrochina.com.cn (X.Z.); hanmguo@petrochina.com.cn (G.H.)
5 Key Laboratory of Tectonics and Petroleum Resources of Ministry of Education, Faculty of Earth Resources, China University of Geosciences, Wuhan 430074, China
* Correspondence: zengjh@cup.edu.cn (J.Z.); jiangsu@cug.edu.cn (S.J.)

Received: 21 August 2019; Accepted: 25 October 2019; Published: 28 October 2019

Abstract: The uncertainties between reservoir quality and gas migration and accumulation in tight sandstone gas reservoirs are intrinsically attributed to complex microscopic pore structures. Integrated analysis including the physical simulation experiment of gas migration and accumulation, X-ray computed tomography (X-CT), and casting thin section (CTS) were conducted on core plug samples collected from the Upper Paleozoic Permian Lower Shihezi and Shanxi tight sandstone of the Daniudi area in the Ordos Basin to investigate the impacts of pore structure on the gas migration and accumulation. Physical simulation suggested that the gas flows in migration in tight sandstone reservoirs were characterized by deviated-Darcy linear flow and non-linear flow regimes. Minimum and stable migration pressure square gradients determined by application of apparent permeability were employed as key parameters to describe gas flow. Pore structure characterization revealed that the tight sandstone reservoir was characterized by wide pore and throat size distributions and poor pore-throat connectivity. The pore–throat combinations could be divided into three types, including the macropore and coarse throat dominant reservoir, full-pore and full-throat form, and meso-small pore and fine throat dominant form. Comparative analyses indicated that pore and throat radii determined the gas flow regimes by controlling the minimum and stable migration pressure gradients. Gas accumulation capacity was dominated by the connected effective porosity, and the gas accumulation process was controlled by the cumulative effective porosity contribution from macropores to micropores. Variations in pore structures resulted in differences in gas migration and accumulation of tight sandstone reservoirs. The macropore and coarse throat-dominant and the full-pore and full-throat reservoirs exhibited greater gas migration and accumulation potentials than the small pore and fine throat dominate form.

Keywords: tight gas sandstone; pore structure; gas migration and accumulation; gas flow

1. Introduction

Tight gas has attracted worldwide attention since the exploration of the large Cretaceous Balnco low-permeability gas field in the San Juan Basin in North America. Tight sandstone gas serves as an important alternative to the conventional petroleum resources and shows good resource prospect [1–3]. Tight sandstone gas has been discovered in more than 70 basins worldwide, which are mainly distributed in North America, Europe, and Asia. The United States and China are two main producers of tight sands gas; the United States has a tight sandstone gas reserve of 42.5×10^{12} m^3 with an annual production of 1754×10^8 m^3 [4,5]. The exploration of tight sandstone gas has developed rapidly in the past decades in China, and prolific tight gas reservoirs have been discovered in the Ordos Basin, Sichuan Basin, and Songliao Basin [6–9].

Tight sandstone gas is generally referred to as the tight sandstone reservoirs with complex gas and water distributions, low gas saturation, and continuous accumulation characteristics [7]. The tight gas sandstone reservoir is defined as gas-bearing sandstone reservoirs with porosity <10%, in situ permeability $<0.1 \times 10^{-3}$ mD or absolute permeability $<1.0 \times 10^{-3}$ mD, gas saturation <60%, and pore-throat radius <1 μm [10–12].

Tight sandstone gas reservoirs are characterized by inter-bedded or closely distributed source rock and reservoirs, small pore and throat radii, high water saturation, and non-tectonic controlled gas distributions [13–16]. The low gas saturation and complex gas and water distributions are the main risks for the exploration and recovery enhancement of tight sandstone gas [17–21]. The gas saturation varies and has a heterogeneous distribution poorly correlated with reservoir quality [22,23]. Porosity and permeability are no longer suitable for the prediction of gas enrichment zones in tight sandstone gas reservoirs. Moreover, gas saturation and distribution are determined by the gas migration and accumulation patterns [24–26]. Due to the nano-micrometer pore system in tight sandstone reservoirs, the capillary pressure increases evidently in tight sandstone. The buoyancy is invalid in driving gas flow and the overpressure becomes the dominant driving force for gas migration [27–30]. Spencer has emphasized that driving pressure difference decides the degrees of gas migration and accumulation in tight sandstone reservoirs [29]. The ultra-high capillary pressure generated by formation water in the pore space becomes the main resistance for the gas migration in tight sandstone reservoirs [10,21,31,32]. As the resistance is determined by the pore geometries, pore structure becomes an important factor for gas migration and accumulation [17]. The heterogeneity of gas saturation and distribution is attributable to the complex microscopic pore structure of tight sandstone reservoirs [33–35]. Therefore, pore structure characterization and gas migration characteristics have become the focus of current studies. Pore size, genesis, morphology, and fractal characteristics have been thoroughly investigated by various techniques including mercury intrusion porosimetry (MIP), scanning electron microscopy (SEM), nuclear magnetic resonance (NMR), low temperature N2 absorption (LTNA), and X-ray computed tomography (X-CT) [36–38]. Recent studies tend to characterize the full-range pore size distribution by integration of several techniques, such as NMR and MIP, LTNA and NMR, and MIP and X-CT [39–41]. These studies provide mature methodology and sufficient information for the pore structure of tight sandstone reservoirs. The gas flow regimes have been clearly stated by experimental and numerical simulations, including the Darcy, high-velocity non-Darcy, and low-velocity non-Darcy flows [42–46]. However, these results are based on the discussions of single-phase fluid flow and have differences with the gas migration process, which is rarely involved. Zeng firstly proposed the minimum migration pressure gradients by investigating the gas flow in migration in tight sandstone reservoirs and indicated that porosity and permeability influences the gas flow patterns, minimum migration pressure gradients, and gas saturation [47]. Moreover, absent evaluations in the relationships between pore structures and gas flows result in uncertainties in the intrinsic microscopic controlling factors for the gas flow in migration. Therefore, combined pore structure characterization and gas migration simulation appear to be necessary in revealing the impacts of pore structure on the gas migration and accumulation.

The Upper Paleozoic Permian Daniudi gas field in the Ordos Basin was chosen as the study area for the heterogeneous reservoir qualities, complicated gas-water distribution, low gas saturation, and their poor internal relationships, which are similar to the tight gas reservoirs in the sedimentary basins in the North Sea and in North America [1,48–52]. In order to reveal the impacts of pore structure on the gas flow in migration and accumulation process in the tight sandstone, physical simulation experiments of gas migration and accumulation combined with X-ray computed tomography (X-CT) and casting thin section (CTS) analyses were conducted on the 13 samples collected from Shanxi and Lower Shihezi formations in the Daniudi gas field. The aims of this paper were as follows: (1) clarifying the gas flow regimes in migration and gas accumulation patterns in the tight sandstone reservoirs, (2) characterizing nano-micrometer scale pore structure of the tight sandstone reservoirs, (3) revealing the intrinsic microscopic controlling factors for gas flow and their impacts on gas migration and accumulation.

2. Geological Settings

The Ordos Basin is an inherited craton basin located in the north of the northern China platform with an area of 25×10^4 km^2. The regional structure appears as a gently western-dipping monocline, which can be divided into six first-order structural units including the Yimeng uplift, the Weibei uplift, the western margin thrust belts, the Shanbei slope, the Tianhuan depression, and the Jinxi flexure belts (Figure 1a) [53,54]. The Upper Paleozoic Permian Shanxi and Lower Shihezi formations are the major gas-bearing layers in the Ordos basin. The transitional facies of barrier coast system and deltaic and fluvial strata constitute a complete source-reservoir-cap assemblage, the coal strata and thick mudstone in the lower part of Shanxi formation act as regional source rock, the deltaic and fluvial sediments are the main reservoir bodies, and the regional continental mudstone deposited in the Upper Shihezi and Shiqianfeng formations forms the regional cap of the whole petroleum system (Figure 1b) [55–57].

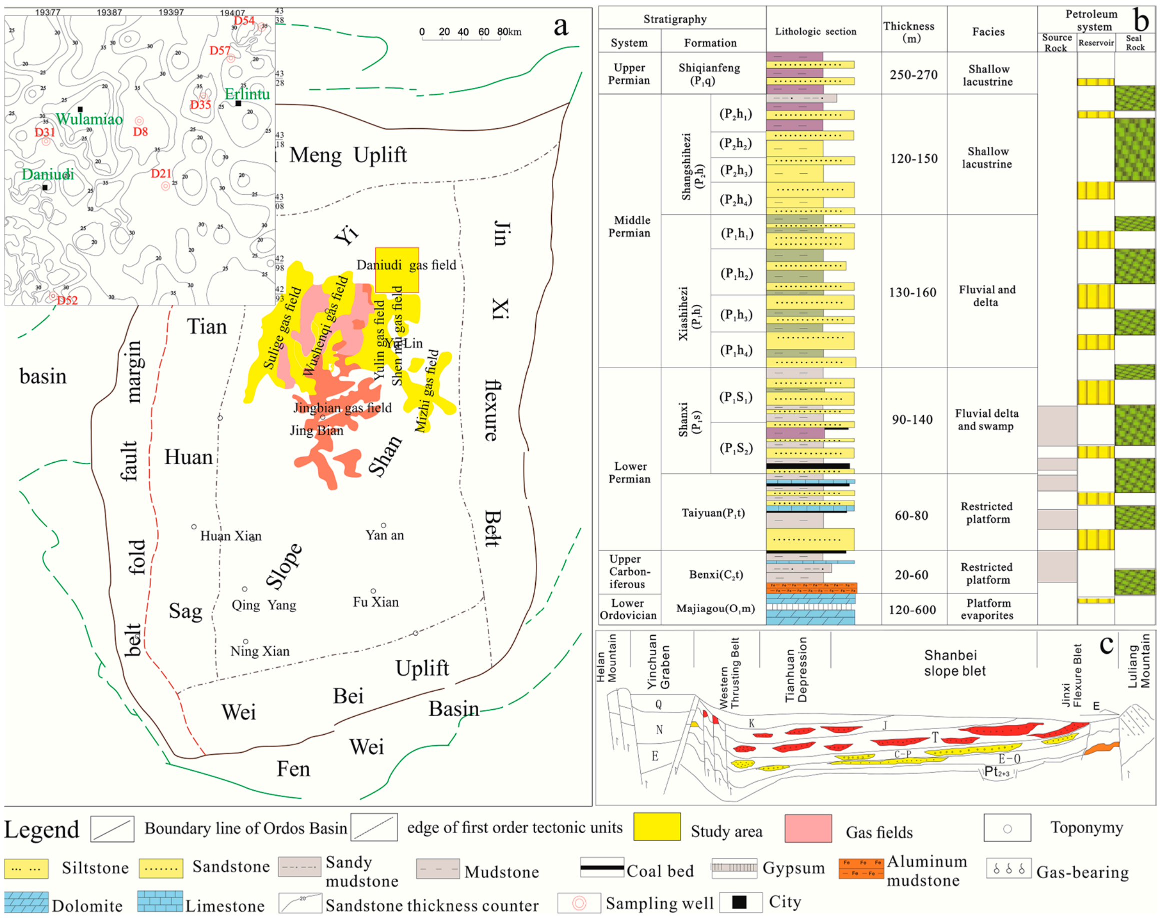

Figure 1. Geological settings of the Daniudi gas field in the Ordos Basin. (**a**) Simplified structural units, Permian tight gas reservoirs distribution, locations of study area and sampling wells in the Ordos Basin. (**b**) Stratigraphic column and petroleum system of the Daniudi area. (**c**) The cross section of hydrocarbon distributions in the Ordos Basin.

The study area, Daniudi gas field, is a typical Upper Paleozoic tight gas reservoir located in the northeastern of the Shanbei slope. The fine sandstone and pebbly medium sandstone formed in the deltaic and fluvial sediments act as the main reservoir bodies of the Shanxi and Lower Shihezi formations [58–60]. The high residual paleopressure in the Carboniferous and Permian source rocks that developed during the late Triassic and early Cretaceous, ranging from 5.0–20.0 MPa, provides the driving forces required for the gas migration in the same period [61]. The tight gas is characterized by low gas abundance, inter-bedded gas layers in longtitude, and planar wide gas distribution [62]. The heterogeneous gas distribution is the main risk for the exploration and development of tight gas [62,63] (Figure 1a,c).

The Permian tight gas sandstone in the study area shares similar geological characteristics, including the co-existence, closely distributed, or interbedded source and reservoir rock, discontinuous reservoir sand bodies, isolated reservoirs in the same formation with low porosity and ultra-low permeability, sequences deposited in shallow marine and fluvial-deltaic environments, and the complex gas–water distributions, with the typical tight sandstone reservoirs in the Upper Jurassic Cotton valley sandstone in east Texas [52], Cretaceous Mesaverde Group in the Piceance Basin [50], and Greater Green River Basin in the Rocky Mountain Basins in America [16], Cretaceous sandstone in the eastern Albert Basin in western Canada [15], and the Dutch sector of the Southern North Sea [49]. Therefore, the same geological scenarios in the Permian tight gas sandstone reservoirs probably can be found in the tight sandstone reservoirs in North America and North Sea, and the study in the Permian tight sandstone reservoirs in the Ordos Baisn may provide insights for the further research on the tight sandstone in the sedimentary basins worldwide.

3. Methods

3.1. Sample Information

Thirteen samples were collected from seven gas-producing wells (Figure 1) in the Upper Paleozoic Permian Shanxi and Lower Shihezi tight sandstone formations in the Daniudi gas field. Cylindrical samples with lengths of ~5.0 cm and diameters of ~2.5 cm were drilled perpendicularly from the fresh core in the wellbore, covering the depths of 2344.80–2804.38 m. The samples mainly consisted of lithic quartz sandstone and litharenite, followed by quartzose sandstone, which are medium-to-coarse grained. The sandstone has a low compositional maturity, with an average quartz content of 73.9%, an average rock fragment content of 19.5%, and a low average feldspar content of less than 3%.

3.2. Experimental Methods

3.2.1. Measurements of Porosity and Permeability

The residual hydrocarbons and salt in the samples were firstly removed using a mixed solution of alcohol and trichloromethane. Then, the samples were dried for 24 h at 120 °C before porosity and permeability measurements [64]. The helium porosity was measured by the helium porosimeter and the permeability was measured by the nitrogen permeation analyzer in the state key laboratory of the China University of Petroleum (Beijing) under a confining pressure of 1.5 MPa, following the standard SY/T 5336-2006 in China, and the information is listed in Table 1. The measuring accuracies of the porosity and permeability determined by the testing instruments were 0.01% with errors of ±0.5%, and 0.001 mD with errors of ±0.1%, respectively.

Table 1. Sample information.

Sample	Formation	Depth (m)	Diameter (cm)	Length (cm)	Porosity (%, ±0.5%)	Permeability (mD, ±0.1%)
S8-14	Shanxi	2636.70	2.44	4.84	3.46	0.004
S31-7	Shanxi	2804.38	2.44	5.58	7.02	0.077
S21-3	Shanxi	2631.20	2.44	5.46	6.65	0.108
S35-5	Shanxi	2547.82	2.44	6.06	8.40	0.186
S21-15	Lower Shihezi	2561.40	2.43	5.12	6.92	0.196
S8-12	Shanxi	2633.20	2.44	5.34	7.66	0.366
S54-11	Lower Shihezi	2257.30	2.43	4.28	6.28	0.442
S31-6	Shanxi	2800.73	2.44	5.13	6.47	0.582
S57-6	Shanxi	2703.05	2.43	5.13	6.67	0.645
S54-3	Shanxi	2344.80	2.43	4.93	8.32	0.689
S35-6	Shanxi	2534.06	2.44	5.53	8.31	0.782
S52-1	Lower Shihezi	2639.40	2.43	5.14	8.92	0.863
S21-8	Shanxi	2607.80	2.43	5.79	9.60	0.989

3.2.2. Physical Simulation of Gas Migration and Accumulation

The physical simulations of gas migration and accumulation were conducted on the samples using the Multiphase Core Flooding instrument in the state key laboratory of the China University of Petroleum (Beijing). The instrument is consisted of fluid intrusion system (ISCO pump), core flooding system (piston container and Hassler core holder), pressure and temperature control system including thermostat, confining pressure pump, back pressure regulator, fluid monitoring and metering system, and automatic data acquisition system (Figure 2).

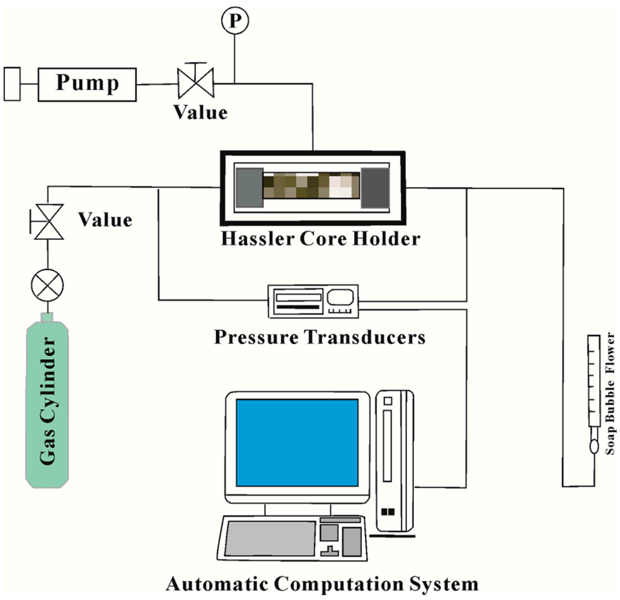

Figure 2. The core flooding facility for physical simulation of gas migration and accumulation.

The core plugs were firstly evacuated and saturated with formation water with a salinity of 50 g/L. The brine-saturated core plugs were placed into the core holder with experimental temperature and confining pressure setting to 85 °C and 22 MPa, respectively, which are consistent with formation pressure and temperature. Nitrogen was employed in the experiment for its similar physical properties compared to natural gas, with a density of 1.16 g/cm^3 and viscosity of 17.54 μPa·s. The pressure transient method was used in the simulation experiments. The inlet pressure was gradually increased and kept constant for a period of time in the beginning stage, and was maintained until a stable velocity of gas flow was detected in the outlet. The pressure differences and stable velocities were recorded, and the accuracies of the injection pressure and fluid flow velocity were 0.001 MPa and 0.001 mL/min, respectively, with errors of ±1%, which were determined by the pressure transducer and flow meter of the flooding instrument. With increasing injection pressure, 10–15 data points were recorded accordingly. The experiment was not stopped until there was no longer water producing in the outlet and the flow velocities of inlet and outlet were equal.

3.2.3. Pore Structure Characterization

After the physical simulation, seven samples with different gas migration and accumulation characteristics were chosen. The samples were evacuated and dried for 12 h at 120 °C before the pore structure characterization analysis. Slices with thickness <3 mm were cut from the top of the core plugs and grinded into thin sections of ~0.3 mm. The thin sections impregnated by blue resin were observed by polarizing optical scope to probe the size, morphology, and fillings of the pores. A total of 10 micrographs were collected for each sample. X-CT scanning was performed on the remaining parts of the seven core plugs using the Zeiss Xradia Versa-510 micro-CT instrument in the state key laboratory of the China University of Petroleum (Beijing). The samples were placed into the micro-CT for scanning with a voltage of 120 kV, a current of 10 μA, a resolution of 2 μm, and a horizon of 5000 × 5000 × 5000 μm^3. A total of 991 tomography images were collected with an exposure time of 20 s and reconstructed to three dimensional (3D) grayscale images using the Zeiss reconstruction software. A representative volume of 500 × 500 × 500 pixels were chosen from the reconstructed 3D images after noise removal using the FEI Avizo Fire 9.0.1. Threshold grayscale segmentation was then performed on the representative volume to separate the pores from rock matrix on the basis of the X-ray absorption differences in the materials with varied density according to the Law of Bill (Equation (1)), and the segmentation process is displayed in Figure 3.

$$I = I_0 e^{-\mu x} \quad (1)$$

where I is photon quantity after X-ray penetration, I_0 is photon quantity before X-ray penetration, and μ is attenuation coefficient.

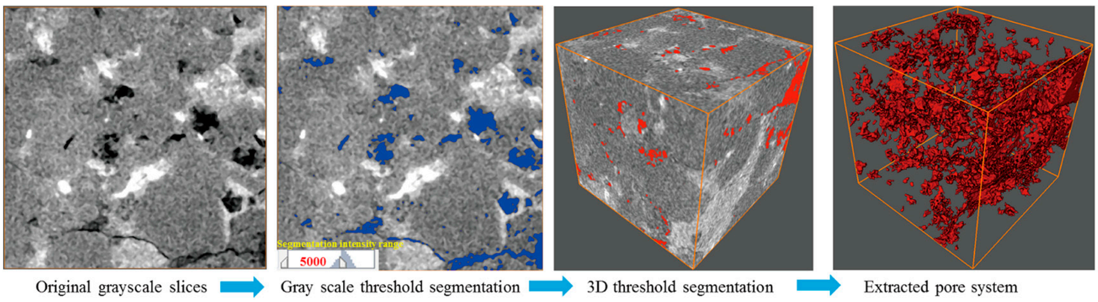

Figure 3. The processing method of threshold grayscale segmentation on X-ray computed tomography (X-CT) scanning results.

The pore network modelling based on the maximum spherical algorithm was employed on the segmentation results to identify the pores and throats, to generate pore network, and to calculate the parameters of pores and throats, including the pore radius, pore volume, throat radius, and coordination number [65–67].

4. Results

4.1. Gas Flow Regimes of Gas Migration in Tight Sandstone Reservoirs

The gas migration in tight sandstone reservoirs is a process in which the natural gas continuously displaces the formation water in the pores and throats under the driving of overpressure. The seepage curves revealed that gas flow in migration deviated from Darcy flow and was characterized by an evident "threshold pressure gradient", which represented the additional pressure gradient required for overcoming the resistance and starting fluid flow (Figure 4). Two flow regimes were found in the gas migration, including a concave seepage curve with non-linear flow in low-velocity stage and linear flow in relative high-velocity stage that can be described by piecewise functions as shown in Equation (2), describing the curved segment on the gas flow curve using the power function and describing the linear segment using the linear function according to the large quantity of experimental results [68], as well as a linear flow curve disjointed to the origin with an intercept on the *x*-axis, which can be described by Equation (3) [69].

$$\begin{cases} v = 0 \quad if\ \frac{\Delta P}{L} \leq a \\ v = \frac{K}{\mu}\left(\frac{\Delta P}{L} - a\right)^2 if \quad a \leq \frac{\Delta P}{L} \leq b \\ v = \frac{K}{\mu}\left(\frac{\Delta P}{L} - c\right) \ if \quad \frac{\Delta P}{L} > b \end{cases}, \tag{2}$$

$$v = \frac{K}{\mu}\left(\frac{\Delta P}{L} - \frac{d\mu}{K}\right), \tag{3}$$

where v is the gas flow velocity, cm/s; $\frac{\Delta P}{L}$ is the pressure square gradient, MPa/cm; K is the nitrogen permeability, cm^2; μ is the viscosity, mPa·s; and a, b, c, and d are constants.

The flow regimes with different tracing pattern exhibit evident distinctions in the threshold pressure gradients and seepage velocities. The linear gas flow generally had a gas flow velocity and a lower threshold pressure square gradient greater than the non-linear gas flow (Figure 4).

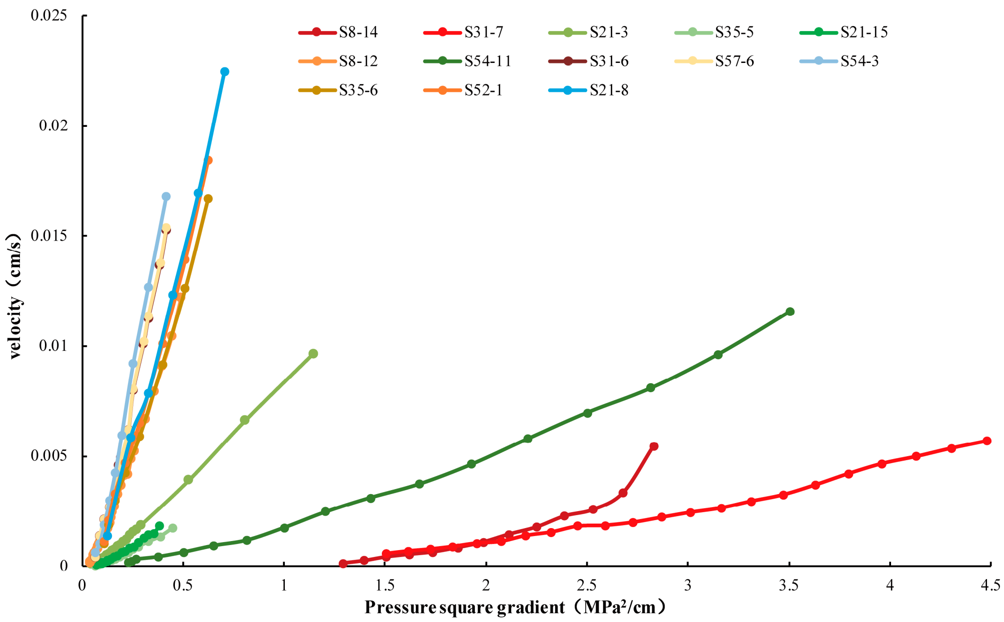

Figure 4. The conventional gas seepage curves of gas flow in migration for the 13 tight sandstone samples.

Threshold pressure gradient has been regarded as a key parameter in characterizing the non-Darcy flow in single-phase gas flow, which is generally calculated by the application of non-Darcy equation and mathematic fitting [42–44,70]. For the linear gas flow, threshold pressure gradient is the intercept of the linear equation on the *x*-axis, and can be replaced by the value of "*d*" in Equation (3). When considering the non-linear gas flow, as any point on the curve follows the non-Darcy flow equation (Equation (4), which is the transformation of Equation (3), Equation (4) can be expanded into Equation (5), and the experimental values of velocity and pressure square gradient can be fitted in the form of Equation (6) according to the non-Darcy flow equation [71].

$$v = \frac{K_e}{10\mu}\left(\frac{\Delta P}{L} - \gamma\right), \tag{4}$$

$$v = \frac{K_e}{10\mu}\cdot\frac{\Delta P}{L} - \frac{K_e\gamma}{10\mu}, \tag{5}$$

$$v = A\left(\frac{\Delta P}{L}\right)^2 + B\left(\frac{\Delta P}{L}\right) + C, \tag{6}$$

where v is the gas flow velocity, cm/s; $\frac{\Delta P}{L}$ is the pressure gradient, MPa/cm; K_e is the nitrogen permeability, cm^2; μ is the viscosity, mPa·s; and A, B, C, and γ are constants.

The positive real root of the fitting equitation if the velocity is assumed to be zero is the "threshold pressure square gradient". However, the physical simulation of gas migration was different from the conventional single-phase gas flow simulation. Although any point on the flow curves follows single-phase gas flow, the water saturation varied between different points, resulting in the limited application of non-Darcy equation in calculating the threshold pressure gradient. The threshold pressure gradient exhibits different physical significance from the common one, representing the minimum pressure square gradient required to displace the formation water in tight sandstone reservoirs. This issue is explained to avoid further conceptual confusion and misapplication.

The apparent permeability provides an effective way to characterize two or multiphase flow in porous media for its accuracy in describing the flow characteristics of single fluid in multiphase flow and would not be affected by the other phase of fluid, which can be calculated by the apparent permeability Equation (7).

$$K_g = \frac{2Q\mu P_0 L}{A\Delta P^2}, \tag{7}$$

$$Kg' = a\ln x + b, \tag{8}$$

where K_g is the gas apparent permeability, cm^2; Kg' is the value of the gas apparent permeability; Q is the quantity of gas flow, ml/s; $x = \frac{\Delta P^2}{L}$ is value of the pressure square gradient; P_0 is the standard atmosphere pressure, MPa; L is the average flow path, cm; A is the area of cross section, cm^2; ΔP is the displacement pressure difference, MPa; and a and b are constants.

With increasing displacement pressure, the gas apparent permeability will vary regularly as the gas migrates into smaller pores by overcoming the corresponding capillary pressure, reflecting the gas flow state in migration. The variations of apparent permeability in the gas flow process can be divided into two segments, in which the gas apparent permeability increases steadily in the beginning stage and then becomes stable in the later stage with the continuously increasing pressure square gradient. According to the analysis of 13 samples (Figure 5), the apparent permeability had a strictly logarithmic correlation with the pressure square gradient in the semi-log coordinate. This correlation can be described by a general fitting equation (Equation (8)) according to the numerical fitting (Table 2). Accordingly, the positive real roots of the fitting equation if the apparent permeability was assumed to be zero were defined as the minimum migration pressure square gradients, representing the minimum driving forces required to start the gas migration in water-saturated tight sandstone reservoirs. The stable gas apparent permeability in the later stage indicated the formation of a main pathway for gas flow in the pore system and corresponded to a secondary large-scale gas migration in the formation scale. Therefore, we defined the minimum pressure square gradient that had a difference of 5% or less with the stable apparent permeability as the stable migration pressure square gradient. The two migration pressure square gradients had errors of ±1%, which were determined by the experiment instruments.

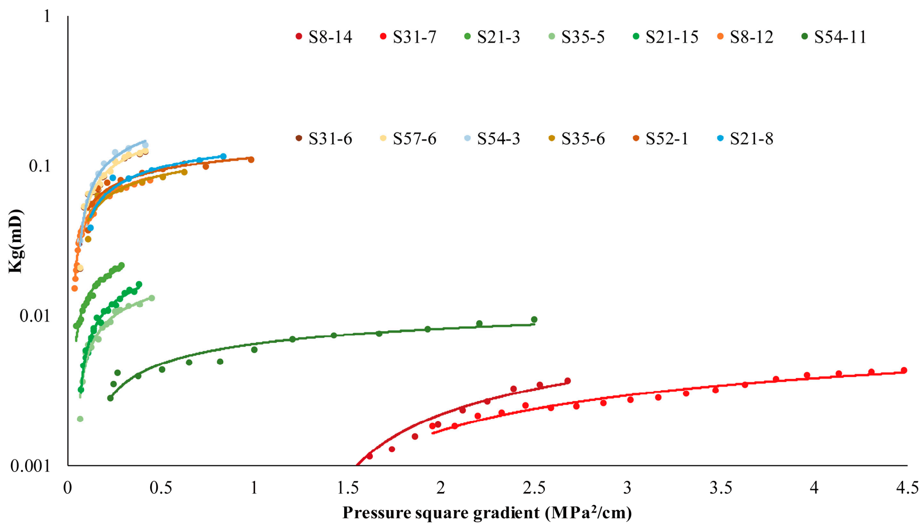

Figure 5. Plots of gas apparent permeability vs. pressure square gradient showing the variations of apparent permeability in the gas migration process.

Table 2. Fitting equations and key migration pressure gradients of gas flow in migration.

Samples	Correlation Formula	Coefficient	Minimum Migration Pressure Square Gradient (MPa^2/cm, ±1%)	Stable Migration Pressure Square Gradient (MPa^2/cm, ±1%)
S8-14	$y = 0.0047\ln(x) - 0.001$	0.9699	1.2370	2.3880
S31-7	$y = 0.0028\ln(x) - 4 \times 10^{-5}$	0.9606	1.0140	3.9600
S21-3	$y = 0.0071\ln(x) + 0.0293$	0.9828	0.0161	0.2521
S35-5	$y = 0.0054\ln(x) + 0.0175$	0.9735	0.0676	0.3282
S21-15	$y = 0.0073\ln(x) + 0.0223$	0.9870	0.0470	0.3049
S8-12	$y = 0.027\ln(x) + 0.1049$	0.9813	0.0205	0.3564
S54-11	$y = 0.0028\ln(x) + 0.0067$	0.9443	0.0913	0.5036
S31-6	$y = 0.0532\ln(x) + 0.173$	0.9639	0.0380	0.3053
S57-6	$y = 0.0537\ln(x) + 0.1745$	0.9639	0.0387	0.3053
S54-3	$y = 0.064\ln(x) + 0.2018$	0.9797	0.0427	0.2538
S35-6	$y = 0.0282\ln(x) + 0.1054$	0.9110	0.0238	0.2859
S52-1	$y = 0.0282\ln(x) + 0.1133$	0.9141	0.0067	0.2137
S21-8	$y = 0.0362\ln(x) + 0.122$	0.9568	0.0196	0.4489

Figure 5 shows that there were two types of apparent permeability variations in the tight sandstone reservoirs, one of which was characterized by low minimum and stable migration pressure square gradients, a rapid growth of apparent permeability, and a high stable apparent permeability, but the other one was characterized by greater migration pressure gradients, a slow-growing pattern of apparent permeability, and a lower stable apparent permeability.

4.2. Gas Accumulation Patterns in the Tight Sandstone Reservoir

As gas migrates into the pore spaces and displaces the formation water in them by overcoming the capillary pressure, the gas will accumulate in the pore space during this procedure and result in gas saturation growth. We proposed a saturation equation to calculate the gas saturation in the cylindrical samples.

$$S_g = \left(1 - \frac{100\% V_w}{\varphi \pi r^2 l}\right) \times 100\% \quad (9)$$

where S_g is the gas saturation, %; φ is the helium porosity, %; r is the radius of samples, cm; l is the length of the samples, cm; and V_w is the cumulative volume of water that are displaced from the outlet under a certain pressure square gradient, cm^3.

The gas saturation exhibited an increasing trend in the beginning stage and became stable with increasing pressure square gradient (Figure 6). However, the growth patterns varied in tight sandstone reservoirs, which can be divided into three types, namely, type I with a small entry pressure square gradient of initial saturation growth, ranging from 0.046 to 0.049 MPa^2/cm, a rapid saturation growth pattern, and a high ultimate gas saturation (maximum saturation that did not grow with the continuously increasing pressure square gradient), ranging from 68 to 92%; type II that was characterized by a greater initial entry pressure square gradient of 0.047–0.081 MPa^2/cm, a rapid-to-slow saturation growth pattern, and a high maximum saturation of 73–92%; and type III with a greatest initial entry pressure square gradient, ranging from 0.18 to 0.21 MPa^2/cm, a slow gas growth pattern, and a lower ultimate gas saturation between 33% and 50% (Figure 6 and Table 3).

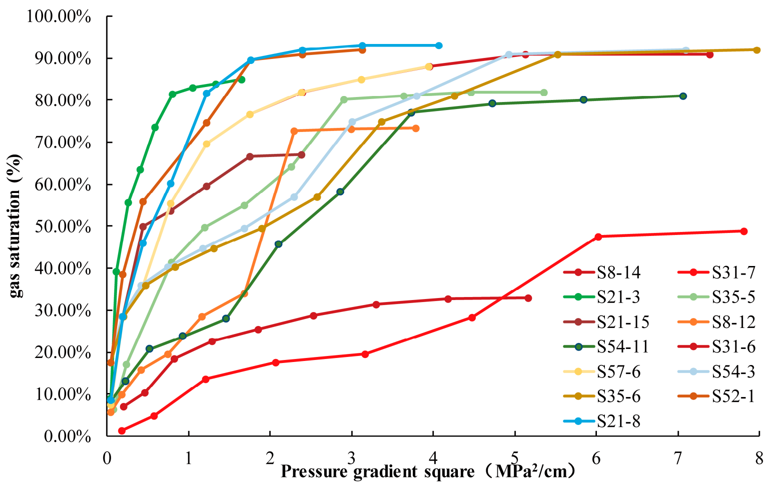

Figure 6. Plots of gas saturation vs. pressure square gradient reflecting the gas accumulation process in tight sandstone reservoirs.

Table 3. The gas accumulation characteristics in tight sandstone reservoirs.

Sample	Ultimate Gas Saturation (%, ±1%)	Initial Gas Growth Pressure Square Gradient from Experiments (MPa^2/cm, ±1%)	Gas Saturation Growth Pattern	Gas Accumulation Type
S8-14	33.0%	0.21	slow saturation growth pattern	III
S31-7	50.0%	0.18	slow saturation growth	III
S21-3	85.0%	0.046	rapid saturation growth	I
S35-5	82.0%	0.081	rapid to slow saturation growth	II
S21-15	68.0%	0.049	rapid saturation growth	I
S8-12	73.0%	0.047	rapid saturation growth	I
S54-11	81.0%	0.058	rapid to slow saturation growth	II
S31-6	91.0%	0.049	rapid saturation growth	I
S57-6	91.0%	0.049	rapid saturation growth	I
S54-3	92.0%	0.047	rapid to slow saturation growth	II
S35-6	92.0%	0.053	rapid to slow saturation growth	II
S52-1	92.0%	0.049	rapid saturation growth	I
S21-8	93.0%	0.049	rapid saturation growth	I

4.3. Pore Structure Characterization of the Tight Sandstone Reservoirs

4.3.1. Pore Types

The casting thin section observation revealed the existence of primary residual intergranular pore, secondary dissolution intergranular and intragranular pores, moldic pore, and intercrystlline pore in the tight sandstone reservoirs. The plane-viewed porosity of tight sandstone was dominated by secondary porosity, which was characterized by dissolution intergranular and intragranular pores, followed by a small amount of intercrystalline pores (Figure 7). The pore types varied between different tight sandstone samples. Primary and dissolution intergranular pores dominated the pore space in the samples of S52-1 (Figure 7a) and S57-6 (Figure 7d). The pore size ranged from 10 to 100 µm. The spatial distribution of the pore system was dominated by connected and superimposed large pores (Figure 8a,b). The dissolution intergranular pores dominated the plane-viewed porosity of the samples of S8-12 (Figure 7b) and S35-6 (Figure 7e), followed by a little amount of dissolution intragranular and intercrystalline pores. The pore size ranged from hundreds of nanometers to dozens of micrometers. The connected and superimposed large pores occupied the main bodies of the pore system, but there were some sparsely distributed pores with tiny size and single color code in the spatial distribution (Figure 8c–e). For the samples of S8-14 (Figure 7c) and S31-7 (Figure 7f), the intergranular porosity reduced evidently, and dissolution intragranular and intercrystalline pores had higher porosity contributions, resulting in declines in pore size. The proportion of tiny pores with sparse and isolated spatial distribution increased (Figure 8f,g). Distinction in pore types was a dominant factor responsible for the differences in pore structures of the tight sandstone reservoirs.

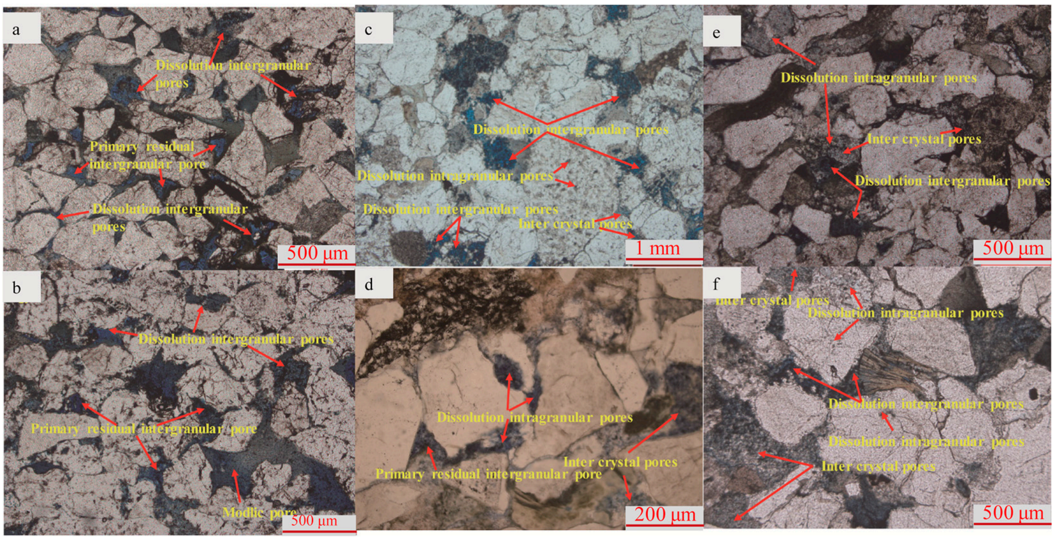

Figure 7. Typical pore types observed by casting thin section observation. Primary and dissolution intergranular pores dominated the plane-viewed porosity in the tight sandstone samples of S52-1 (**a**) and S57-6 (**b**). Plane-viewed porosity was dominated by the dissolution intergranular pores, followed by a little amount of dissolution intragranular and intercrystalline pores in the samples of S8-12 (**c**) and S35-6 (**d**). Evident porosity loss occurred in the sample of S8-14 (**e**) and S31-7 (**f**) due to compaction and cementation, the intergranular pores decreased sharply, and dissolution intragranular and intercrystalline pores had higher porosity contributions in pore system (the interpretation is given by red arrows and yellow annotations in the figure).

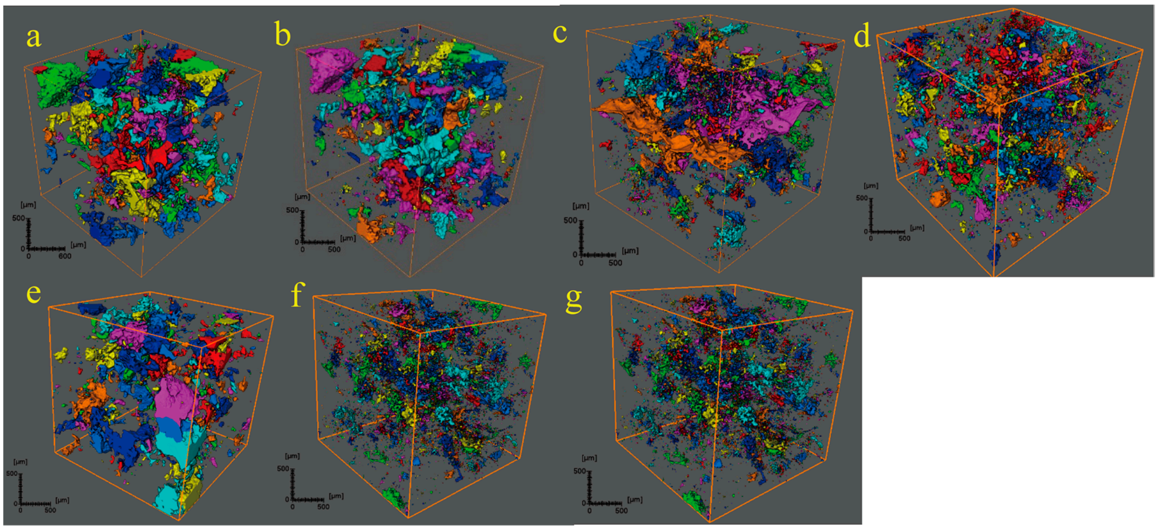

Figure 8. The 3D pore spatial distribution images of seven tight sandstone samples obtained by grayscale segmentation: (**a**) S52-1, (**b**) S57-6, (**c**) S8-12, (**d**) S54-11, (**e**) S35-6, (**f**) S31-7, and (**g**) S8-14 (the irregular bodies in 3D are the pores in the rocks, which are separated by different color labels in the pore system. Same color labels indicate connected pores in adjacent areas).

4.3.2. Pore and Throat Size Distributions

The pore and throat size distributions refer to the frequency distribution of different-sized pore and throats. The pore and throat radii obtained from pore network modelling suggested that the pores in tight sandstone reservoirs had a wide distribution between several hundreds of nanometers and several hundreds of micrometers (Figure 9a). There are many ongoing studies on the pore classification in the tight sandstone reservoirs, and the pores are generally divided by pore sizes and their quantitative proportions. International Union of Pure and Applied Chemistry (IUPAC) divided the pores into micropores (<2 nm), mesopores (2–50 nm), and macropores (>50 nm) [72]. Loucks extended the classification in siltstone and classified the pores into nanopores (1 nm−1 µm), micropores (1–62.5 µm), and mesopores (>62.5 µm) [73]. Qiao further extended the Loucks classification by combining previous studies with his studies on the tight sandstone in the Ordos Basin and divided the pores into four categories, including micropores (<2 µm), small pores (2–10 µm), mespores (10–20 µm), and macropores (>20 µm) [53]. It is apparent that the classifications of IUPAC and Loucks will result in disproportions of the mesopores, and the classification proposed by Qiao appears to be appropriate in describing the pore types in tight gas sandstone of the study area according to the thin section observations and pore size distributions. Additionally, we proposed Equation (10) to evaluate the porosity contribution of different types of pores.

$$P = \frac{\sum_{i=1}^{n} V_i}{V_t} \times 100\% \tag{10}$$

where P is the porosity contribution, %; V_i is the volume of every single pore in different pore types in the interest volume of the rock sample, µm^3; n is the quantity of the pores in specific pore types; and V_t is the total volume of pores in the interest volume of the rock sample, µm^3.

The pore radius concentrated in the range of 2–20 µm, indicating that mesopores and small pores were dominant in terms of quantity. The pore size distribution also varied in different tight sandstone samples. In the samples of S52-1 and S57-6, the pores distributed in the range 500 nm–200 µm and were dominated by small pores and mesopores and followed by macropores in terms of quantity. The results indicated that the macropores had a dominant porosity contribution of more than 99% in the two samples. Taking both of the quantitative proportions and porosity contributions into consideration, the reservoirs were defined as the macropore dominant type. In the samples of S35-6, S8-12, and S54-11, the proportions of small pores and micropores increased, whereas those of macropores and mesopores decreased. The average porosity contributions of macropores, mesopores, small pores, and micropores were 72.33%, 22.31%, 5.18%, and 0.074%, respectively. These reservoirs can be classified as the full pore type. For the samples of S8-14 and S31-7, the pores were dominated by small pores (61.54%) in terms of quantity, with evident reductions in macropores (3.35%) and mesopores (26.08%). The mesopores and small pores had dominant average porosity contributions of 57.77% and 22.44%, respectively. These reservoirs were regarded as the meso-small pore dominant type (Table 4).

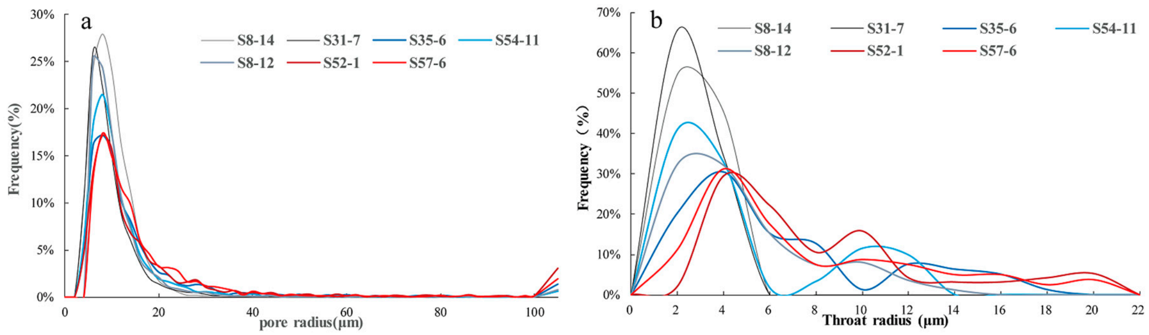

Figure 9. The pore size distributions (**a**) and the throat size distributions (**b**) of the seven chosen samples obtained from pore network modeling.

Table 4. Pore types, proportions, and porosity contributions in the pore systems.

Sample	Macro-Pore (Proportion/ Porosity Contribution, %)	Meso-Pore (Proportion/ Porosity Contribution, %)	Small-Pore (Proportion/ Porosity Contribution, %)	Micro-Pore (Proportion/ Porosity Contribution, %)	Type of Pore System
S52-1	20.29/99.33	28.92/0.55	46.13/0.12	4.65/0.001	Macropore dominant
S57-6	19.75/99.05	35.19/0.80	45.06/0.0016	0/0	Macropore dominant
S35-6	15.39/70.63	30.31/23.90	48.62/5.37	5.67/0.10	Full-pore
S8-12	15.01/69.86	33.71/25.11	47.10/4.96	4.19/0.07	Full-pore
S54-11	11.54/76.50	25.56/17.93	56.94/5.48	5.96/0.053	Full-pore
S8-14	1.94/23.59	30.26/54.98	59.74/21.07	8.06/0.36	Meso-small pore dominant
S31-7	4.76/14.99	21.90/60.56	63.33/23.81	10.20/0.64	Meso-small pore dominant

The throat radius had a continuous distribution between several hundreds of nanometers and dozens of micrometers, concentrating in 500 nm–10 μm, having three kinds of throats in existence according to the classification proposed by Qiao [53], including fine throats with radius between 500 nm and 1μm, medium throats with radius ranging from 1 and 3 μm, and coarse throat with radius greater than 3 μm (Figure 9b). The throat radius distribution varied between different tight sandstone reservoirs. In the samples S52-1 and S57-6, the throat concentrated in the range between 2 and 20 μm and was dominated by coarse throat (average 62.96%), followed by medium throat (average 30.36%), which can be defined as the coarse throat dominant reservoir in terms of quantity. In the samples S35-6, S8-12, and S54-11, the throat radii decreased to the range of 2–14 μm, and average proportions of medium and fine throats increased. The coarse, medium, and fine throats all primarily contributed to the throats. These samples could be regarded as the full throat reservoir. With regard to the samples S8-14 and S31-7, the throat radii mainly distributed in the range 2–4 μm, and fine throat dominated the throats with an average proportion of 60.06%. There were no coarse throats, and there was a relatively small amount of medium throats in the reservoirs (average 39.94%). Thus, they can be defined as the fine throat-dominant reservoir (Table 5).

Table 5. Throat types and their proportions in tight sandstone reservoirs.

Sample	Fine-Throat (%)	Meso-Throat (%)	Coarse-Throat (%)	Type of Throat System
S52-1	2.11	29.47	68.42	Coarse throat dominant
S57-6	11.25	31.25	57.50	Coarse throat dominant
S35-6	20.25	30.38	49.37	Full-throat
S8-12	43.41	23.95	32.34	Full-throat
S54-11	40.98	32.79	26.23	Full-throat
S8-14	54.61	45.39	0	Fine throat dominant
S31-7	65.51	34.49	0	Fine throat dominant

4.3.3. Pore–Throat Connectivity

The skeleton models (Figure 10) indicated that the pore network connectivity of tight sandstone was poor, with low average coordination number ranging from 0.015 to 0.109 and high pore-throat ratio between 2.60 and 4.86 (Table 6). The results revealed a positive relationship between pore size and coordination number in the tight sandstone reservoirs. Macropores were generally connected by several to tens of throats, mesopores were connected with 6–10 throats, small pores were generally connected with 4–6 throats, and micropores were partly connected by 1–2 throats or no throats (Figure 10a,b). The macropore-dominant samples S52-1 and S57-6 (Figure 10a,b) with an average coordination number of 0.096 and a pore–throat ratio of 2.62, having better connectivity when compared with the full-pore form (S35-6, S8-12, and S54-11) with a coordination number of 0.067 and a ratio of 2.87 (Figure 10c–e), and the small pore-dominant form with an average coordination number of 0.016 and a ratio of 4.78 (Figure 10f,g).

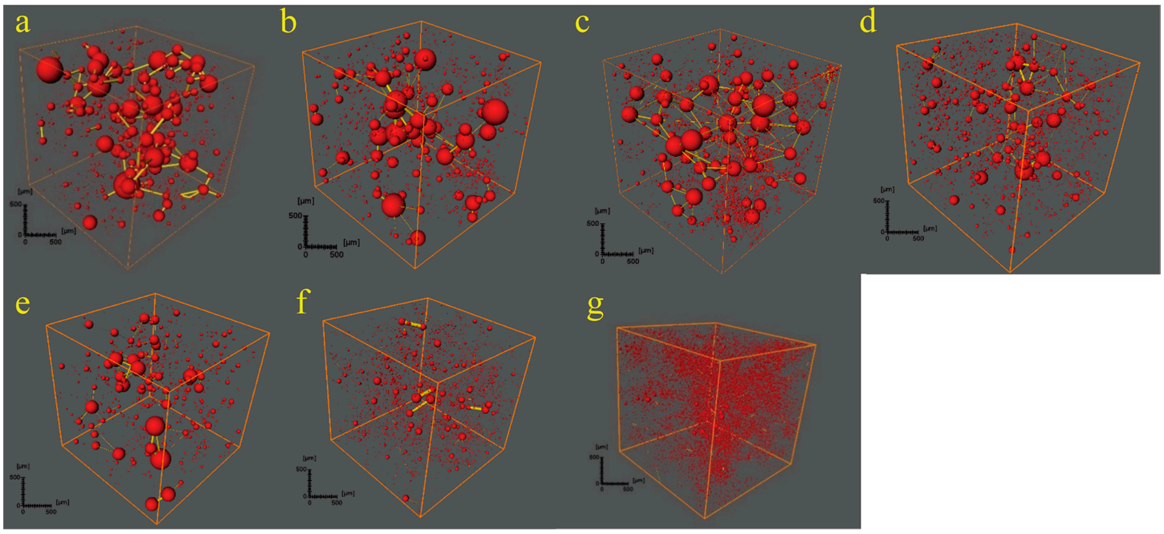

Figure 10. The 3D images of nano-micrometer pore network models showing the pore–throat connectivity and pore–throat combinations of the seven samples: (**a**) S52-1, (**b**) S57-6, (**c**) S8-12, (**d**) S54-11, (**e**) S35-6, (**f**) S31-7, and (**g**) S8-14 (the red balls represent pores with varied radii, the yellow sticks represent the throats with different radius and length).

The tortuosity of the seven samples are calculated according to the Tortuosity Equation (11).

$$\tau = \frac{\varphi D_P}{6(100\% - \varphi)} \sqrt{\frac{\frac{\varphi}{100\%}}{2K}} \quad (11)$$

where τ is tortuosity; φ is the helium porosity, %; D_P is the average pore diameter, µm; and K is the nitrogen permeability, cm^2.

The results suggest a highly circuitous micro-nanometer pore network in the tight sandstone reservoir, indicating multiple flow paths for gas migration. The meso-small pore dominant reservoir had an higher average tortuosity of 52.09 compared with the full-pore form (S8-12, S35-6, and S54-11), with an average of 38.68, and macropore dominant form (S52-1 and S57-6), with an average of 45.93 (Table 6).

4.3.4. Pore Structure Parameters and Pore–Throat Combinations

The detailed pore structure parameters such as average pore and throat radii, average coordination number, average pore-throat ratio, and tortuosity are listed in Table 6. On the basis of the combination of pore and throat, the micro-nanometer pore networks of the seven samples can be classified into three categories, including the macropore and coarse throat dominant type, full-pore and full-throat type, and meso-small pore and fine throat dominant type (Table 6).

Table 6. Pore structure parameters and pore-throat combinations in tight sandstone reservoirs.

Sample	Average Pore Radius (μm)	Average Throat Radius (μm)	Average Coordination Number	Pore-Throat Ratio	Tortuosity	Connected Effective Porosity from X-CT (%)	Pore-Throat Configuration
S52-1	18.90	7.25	0.11	2.61	48.89	7.64	Macropore and coarse throat dominant
S57-6	17.33	6.58	0.083	2.63	42.98	7.04	Macropore and coarse throat dominant
S35-6	15.06	5.59	0.059	2.69	37.63	5.69	Full-pore and full-throat
S8-12	16.25	6.11	0.098	2.83	38.13	6.05	Full-pore and full-throat
S54-11	11.88	3.85	0.044	3.09	40.29	5.14	Full-pore and full-throat
S8-14	8.94	1.90	0.016	4.71	65.69	0.47	Meso-small pore and fine throat dominant
S31-7	9.09	1.87	0.015	4.86	38.50	3.04	Meso-small pore and fine throat dominant

5. Discussion

5.1. The Impacts of Pore Structure on Gas Migration

Porosity and permeability have been considered as the important factors influencing the gas migration and accumulation in low-permeability reservoirs. Previous publications suggest that the seepage curves and threshold pressure gradients vary regularly with the variations of permeability and porosity of low-permeability reservoirs [23,74,75], whereas some others have argued there is no regular correlations between porosity and gas flow characteristics. The results confirmed that the seepage curves deviated to the pressure square gradient axis with decreasing permeability, and that the gas flow patterns changed from linear flow to non-linear flow simultaneously (Figure 4). However, the impact of porosity was irregular. The minimum and stable migration pressure square gradients were poorly correlated with the porosity (Figure 11a) and permeability (Figure 11b) with coefficients less than 0.80, indicating that porosity and permeability were not the intrinsic controlling factors for gas migration (Figure 11).

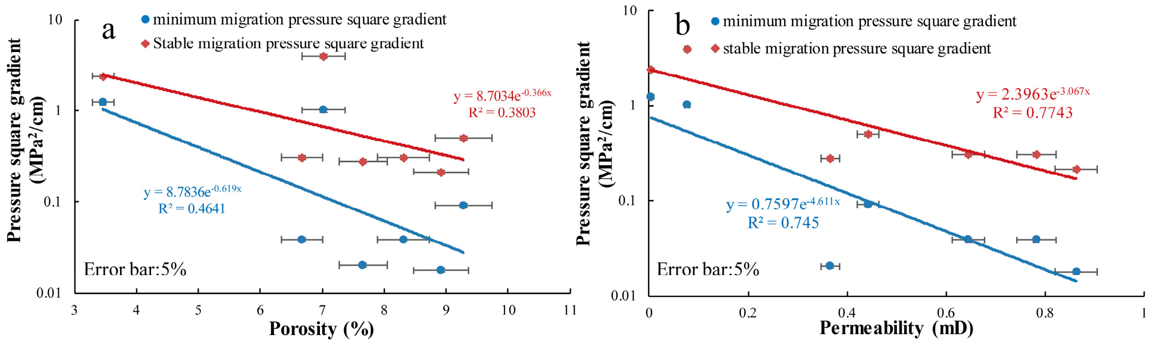

Figure 11. The correlations between porosity, permeability, and gas migration gradients. (**a**) The correlations between minimum migration pressure square gradient, stable migration pressure gradient, and porosity. (**b**) The correlations between minimum migration pressure square gradient, stable migration pressure gradient, and permeability.

The poor correlations between porosity, permeability, and gas migration are intrinsically attributed to the heterogeneous microscopic pore structure of tight sandstone reservoirs [35,45,76–78]. Strong negative correlations between the two key migration pressure square gradients and average pore and throat radii (Figure 12a,b) indicated that the pore and throat radii directly controlled the gas flow in migration, and greater pore and throat radii were favorable for the gas flow in migration. The results agreed with the Washburn Equation [79], in which the pore–throat radius is one of the dominant factors controlling the capillary pressure. With increasing pore and throat radii, it became much easier for gas to migrate into the pore space and to form a stable flow steam in the pore system due to resistance reductions. Moreover, throats exhibited influences on gas migration stronger than the pores because the throats were much narrower than the pores connected to them and could determine the resistance of gas flow between pores, which was supported by the higher correlation coefficient (Figure 12a,b). Both of the two migration pressure gradients had positive correlations with pore–throat ratio (Figure 12c), suggesting that high pore–throat differences were unfavorable for the gas flow between pores due to the increases in capillary pressure differences between pore and throat spaces.

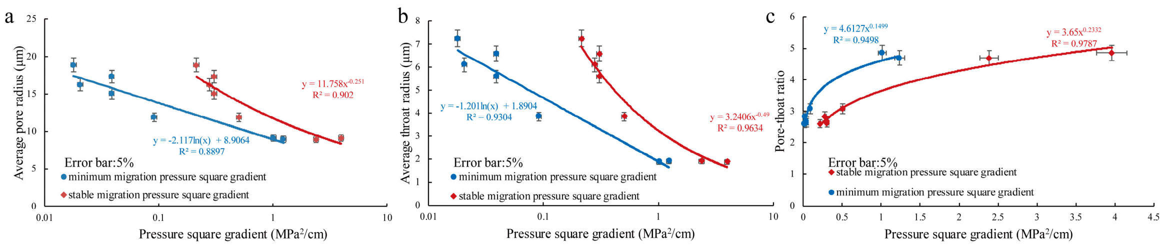

Figure 12. The impacts of pore structure on gas migration: the correlations between average pore radius (**a**), average throat radius (**b**), average pore-throat ratio (**c**), and migration pressure square gradients.

The strong impacts of pore structure parameters on gas flow in migration consequently resulted in close relations between pore–throat combinations and gas migration characteristics. The gas migrated in a deviated Darcy linear flow regime with lower minimum and stable migration pressure gradients in the macropore and coarse throat dominant and full-pore and full-throat reservoirs, but had a non-linear flow regime with higher migration pressure gradients in meso-small pore and fine throat dominant reservoir (Table 7).

Table 7. The relationships between pore–throat combinations and gas migration and accumulation characteristics.

Samples	Pore–Throat Configuration	Gas Flow Pattern in Migration	Gas Accumulation Pattern	Minimum Migration Pressure Square Gradient (MPa^2/cm)	Stable Migration Pressure Square Gradient (MPa^2/cm)	Ultimate Gas Saturation (%)
S52-1	Macropore and coarse throat dominant	Deviated Darcy linear flow	rapid saturation growth	0.0067	0.2137	92.00%
S57-6	Macropore and coarse throat dominant	Deviated Darcy linear flow	rapid saturation growth	0.0387	0.3053	91.00%
S35-6	Full-pore and full-throat	Deviated Darcy linear flow	rapid to slow saturation growth	0.0238	0.2859	92.00%
S8-12	Full-pore and full-throat	Deviated Darcy linear flow	rapid to slow saturation growth	0.0205	0.3564	73.00%
S54-11	Full-pore and full-throat	Deviated Darcy linear flow	rapid to slow saturation growth	0.0913	0.5036	81.00%
S8-14	Small pore and fine throat	Non-linear flow	slow saturation growth	1.2370	2.3880	33.00%
S31-7	Small pore and fine throat	Non-linear flow	slow saturation growth	1.0140	3.9600	50.00%

5.2. The Impacts of Pore Structure on Gas Accumulation

5.2.1. The Impacts of Pore Structure on the Capacity of Gas Accumulation in Tight Sandstone Reservoirs

The risking factors of tight gas exploration lay in the unpredictable relations between gas saturation, permeability, and porosity. The ultimate gas saturation, the maximum gas saturation value that derived from the simulation experiments, represented the gas storage capacity of tight sandstone reservoirs if the driving forces always met the requirements. The ultimate gas saturation had a strong positive correlation with permeability (Figure 13a) but was relatively poorly correlated with porosity, suggesting that the gas storage capacity was determined by the connected pores (Figure 13b). On the basis of the analysis method of effective and ineffective pores proposed by Zeng et al. 2017 [35], the ineffective pores with a coordination number of zero were removed and the volume fraction of connected pores in the interest area of micro-CT results, namely, the effective porosity, were calculated (Table 6). The results suggested that the gas storage capacity had a strong positive correlation with the connected effective porosity, also indicating that the existence of disconnected ineffective pores was the main factor responsible for the poor relationships between porosity and gas saturation (Figure 13b). With increasing pore and throat radii, the decreases in the difficulties of gas flow and the increases of proportion of connected pores in the pore system would result in enhancement in the gas accumulation capacity of the tight sandstone reservoirs. Therefore, great pore and throat radii were favorable for the gas storage capacities of the tight sandstone reservoirs (Figure 13c). It can be further inferred that the macropore and coarse throat dominant and the full-pore and full-throat reservoirs had better accumulation capacities than the meso-small pore and fine throat dominant form (Table 7).

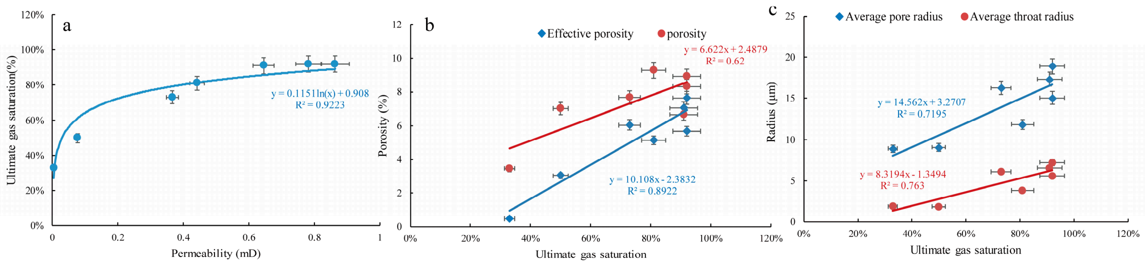

Figure 13. The impacts of reservoir quality and pore structure on the accumulation capacity of tight sandstone reservoirs: (**a**) Plots of permeability vs. ultimate gas saturation. (**b**) Plots of ultimate gas saturation vs. porosity and calculated effective porosity derived from pore network modeling, respectively. (**c**) The correlations between ultimate gas saturation, average pore, and average throat radii.

5.2.2. The Control of Pore Structure on the Process of Gas Accumulation

The gas saturation grew as gas occupied more pore space with increasing pressure square gradient, but the growth pattern varied. The initial saturation growth pressure square gradient reflected the degree of gas accumulation difficulty, and its negative correlations with the average pore and throat radii confirmed that greater pore–throat radii were favorable for the gas accumulation (Figure 14). As gas saturation growth is a process in which gas accumulates in pores with different volumes, the pore size distribution was no longer suitable in evaluating the gas saturation growth process. Therefore, we proposed a method to calculate the effective porosity contributions of pores with different sizes (Equation (12)) and plot the cumulative curve of effective porosity contributions from marcopores to micropores (Figure 15a).

$$\varphi_c = \frac{\sum_{i=1}^{n} V_i}{V_{tc}} \times \varphi_e \qquad (12)$$

where φ_c is the effective porosity contribution, %; V_i is the pore volume of every single connected pores in the corresponding pore types, μm^3; n is the quantity of pores in the specific pore type; V_{tc} is the total pore volume of connected pores in the interest area, μm^3; and φ_e is the effective porosity derived from calculation of X-ray computed tomography, %.

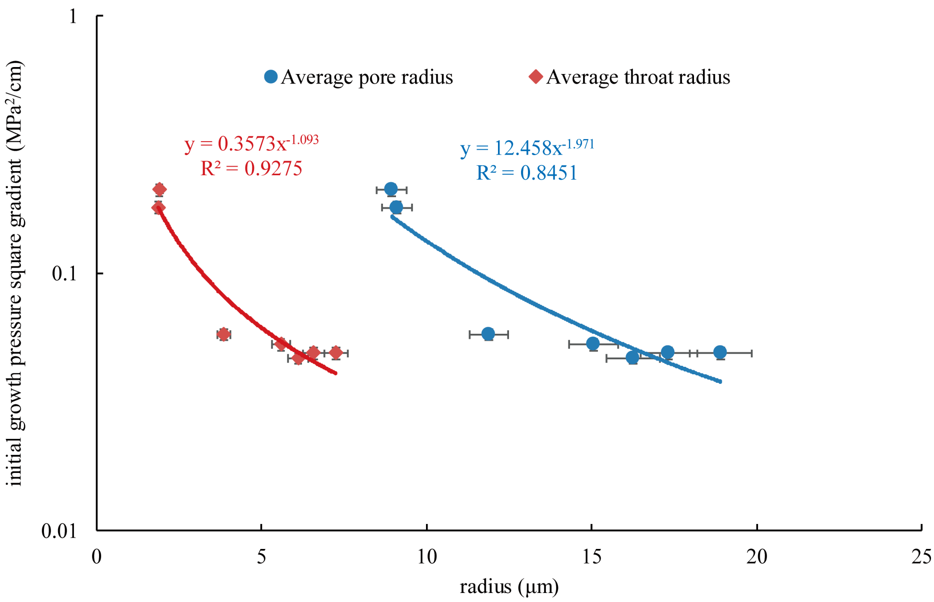

Figure 14. The impacts of pore structure on the degrees of gas accumulation difficulty—plots of entry pressure gradient of initial gas saturation growth vs. average pore and throat radii.

A high consistence has been revealed when comparing the effective porosity cumulative curve (Figure 15a) with the gas saturation growth curve of the same sample (Figure 15b). In the meso-small pore dominant reservoirs of S8-14, the cumulative curve of effective porosity contribution from macropores to micropores experienced a slow growth stage before it became stable (blue line in Figure 15a) and was consistent with its slow gas saturation growth pattern (green line in Figure 15b). Low porosity contribution of macropores and high contributions of mesopores and small pores would result in reductions in pore and throat radii and further lead to a greater increase of pressure square gradient required for a same incremental saturation growth, and a slower saturation growth rate. In the full-pore reservoir of S54-11, the cumulative curve experienced a rapid-slow growth pattern before it became stable (green line in Figure 15a), which was consistent with the gas saturation growth pattern (red line in Figure 15b). As the macropores, mesopores, and small pores played important roles in porosity, the gas saturation experienced a rapid growth period in the beginning stage as gas firstly migrated into macropores and mesopores and then slow down due to the capillary pressure increase caused by small pores and micropores. The small pores and micropores resulted in a larger pressure square gradient required for the same incremental saturation growth in the later stage. For the macropore-dominant reservoir of S52-1, the cumulative curve of effective porosity contribution experienced a rapid linear growth pattern (red line in Figure 15a). The same growth pattern was also found in the saturation growth curve (blue line in Figure 15b). As the dominant macropore porosity evidently decreased the incremental driving force required for the same incremental gas saturation growth, the gas saturation exhibited a rapid growth rate compared with the other two types of reservoirs. The differences in the effective porosity contributions of different pore types controlled the variations in the gas growth patterns of the tight sandstone reservoirs (Figure 15). It can be further inferred that the cumulative curves of effective porosity contributions from macropores to micropores can be employed to predict the ideal gas growth models in the tight sandstone reservoirs.

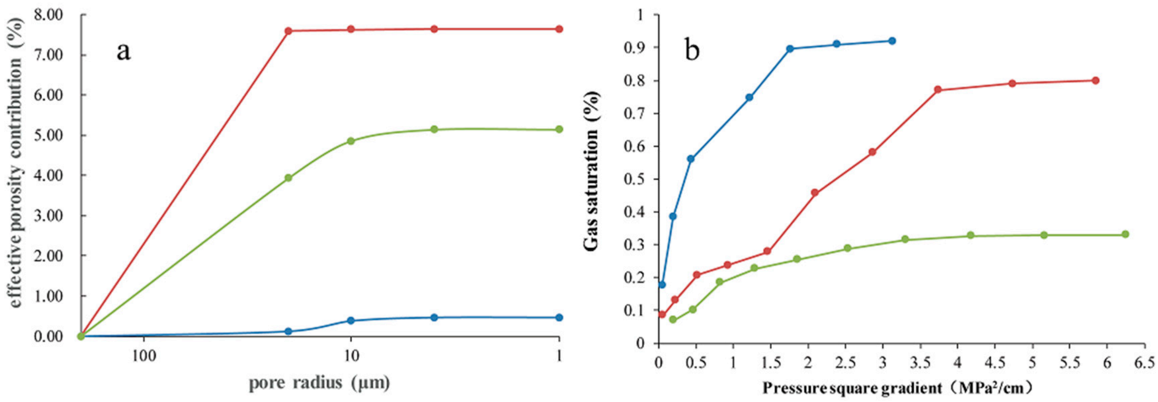

Figure 15. The cumulative curves of effective porosity contribution of pores from macropores to micropores (**a**) and the gas saturation growth curves (**b**) indicating the control of pore structure on the process of gas accumulation in tight sandstone reservoirs.

6. Conclusions

Through the combined studies of the gas migration and accumulation simulation and pore characterization on the tight sandstone reservoirs of the Upper Paleozoic Permian in the Daniudi gas field, Ordos Basin, the conclusions can be drawn as follows:

(1) There were two gas flow regimes in gas migration including the deviated Darcy linear flow and non-linear flow in tight sandstone gas reservoirs. The minimum migration pressure square gradient and the stable migration pressure gradient were identified as two key parameters in describing the gas flow states by the application of gas apparent permeability.

(2) Three different gas saturation growth patterns were discovered in the process, including the rapid saturation growth model with high ultimate gas saturation, the rapid-to-slow saturation growth

model with high ultimate gas saturation, and the slow saturation growth model with low ultimate gas saturation. The ultimate gas saturation directly reflected the capacity of gas accumulation in tight sandstone reservoirs.

(3) The tight gas sandstone reservoirs were characterized by wide pore and throat distributions. Four pore types, including the micropore, small pore, mesopore, and macropore, and three throat types, including the fine, medium, and coarse throats, were identified in the pore system. The macropore and coarse throat dominant reservoir, full-pore and full-throat form, and the meso-small pore and fine throat dominant form were three main pore–throat combinations in tight sandstone reservoirs.

(4) The unpredictable relationships between gas flow, porosity, and permeability were attributed to the complex pore structures. Average pore and throat radii were the microscopic controlling factors for the gas migration. The pore–throat ratio influenced gas migration by affecting the gas flow between pore and throat. Deviated Darcy linear flow commonly occurred in the macropore and coarse throat-dominant and full-pore and full-throat reservoirs, whereas non-linear flow generally occurred in the meso-small pore and fine throat dominant reservoir.

(5) The connected effective porosity determined the gas accumulation capacity in tight sandstone reservoirs. The macropore and coarse throat dominant reservoir exhibited the highest gas accumulation potential among the three types of reservoirs. The cumulative porosity contributions of different pore types determined the gas accumulation process and were responsible for the differences in gas growth patterns. The cumulative curves of porosity contributions from macropores to micropores can be further applied to the prediction of ideal gas accumulation models in tight sandstone reservoir.

Author Contributions: Methodology, J.Q.; investigation, X.Z., S.J. and G.H.; supervision, J.Z.; formal analysis, S.F. and X.F.

Funding: This research was funded by National Natural Science Foundation of China, grant number 41330319 and the Article Processing Charges (APC) was funded by 41330319.

Acknowledgments: This study is supported by the National Natural Science Foundation of China (grant no. 41330319). We sincerely appreciate all anonymous reviewers and the handling editor for their comments and suggestions.

Conflicts of Interest: The authors declare no conflict of interest.

References

1. Holditch, S.A. Tight gas sands. *J. Petrol. Technol.* **2006**, *58*, 86–93. [CrossRef]
2. Silver, C. The occurrence of gas in the Cretaceous rocks of the San Juan Basin, New Mexico and Colorado. In Proceedings of the New Mexico Geological Society, First Field Conference, Santa Fe, NM, USA, 3–5 November 1950.
3. Wei, G.; Zhang, F.; Li, J.; Yang, S.; Huang, C.; She, Y. New progress of tight and gas accumulation theory and favorable exploration zones in China. *Nat. Gas Geosci.* **2016**, *27*, 199–210.
4. Dudley, B.; Dale, S. *BP Statistical Review of World Energy*; BP Company: London, UK, 2012.
5. Tong, X.G.; Guo, B.C.; Li, J.Z.; Huang, F.X. Comparison study on accumulation & distribution of tight sandstone gas between China and the United States and its significance. *Eng. Sci.* **2012**, *6*, 1.
6. Jia, C.Z.; Zheng, M.; Zhang, Y. Unconventional hydrocarbon resources in China and the prospect of exploration and development. *Petrol. Explor. Dev.* **2012**, *39*, 139–146. [CrossRef]
7. Dai, J.X.; Ni, Y.Y.; Wu, X.Q. Tight gas in China and its significance in exploration and exploitation. *Petrol. Explor. Dev.* **2012**, *39*, 277–284. [CrossRef]
8. Zou, C.; Zhu, R.; Liu, K.; Su, L.; Bai, B.; Zhang, X.; Yuan, X.; Wang, J. Tight gas sandstone reservoirs in China: Characteristics and recognition criteria. *J. Petrol. Sci. Eng.* **2012**, *88*, 82–91. [CrossRef]
9. Zou, C.; Zhu, R.; Wu, S.; Yang, Z.; Tao, S.; Yuan, X.; Hou, L.; Yang, H.; Xu, C.; Li, D. Types, characteristics, genesis and prospects of conventional and unconventional hydrocarbon accumulations: Taking tight oil and tight gas in China as an instance. *Acta Petrol. Sin.* **2012**, *33*, 173–187.
10. Guo, Y.; Pang, X.; Chen, D.; Jiang, F.; Tang, G. Progress of research on hydrocarbon accumulation of tight sand gas and several issues for concerns. *Oil Gas Geol.* **2013**, *34*, 717–724.

11. Li, J.Z.; Guo, B.C.; Zheng, M.; Yang, T. Main types, geological features and resource potential of tight sandstone gas in China. *Nat. Gas Geosci.* **2012**, *23*, 607–615.
12. Zou, C.; Tao, S.; Hou, L. *Unconventional Oil and Gas Geology*; Geological Publishing House: Beijing, China, 2011; pp. 269–271.
13. Cant, D.J.; Ethier, V.G. Lithology-dependent diagenetic control of reservoir properties of conglomerates, Falher Member, Elmworth Field, Alberta. *AAPG Bull.* **1984**, *68*, 1044–1054.
14. Gies, R.M. Case history for a major Alberta deep basin gas trap: The Cadomin Formation. *AAPG Memoir* **1984**, *A013*, 115–140.
15. Masters, J.A. Deep basin gas trap, western Canada. *AAPG Bull.* **1979**, *63*, 152–181.
16. Spencer, C.W. Review of characteristics of low-permeability gas reservoirs in western United States. *AAPG Bull.* **1989**, *73*, 613–629.
17. Berkenpas, P. The Milk River shallow gas pool: Role of the updip water trap and connate water in gas production from the pool. In Proceedings of the SPE Annual Technical Conference and Exhibition, Dallas, TX, USA, 6–9 October 1991.
18. Meng, D.W.; Jia, A.L.; Ji, G.; He, D.B. Water and gas distribution and its controlling factors of large scale tight sand gas fields: A case study of western Sulige gas field, Ordos Basin, NW China. *Petrol. Explor. Dev.* **2016**, *43*, 663–671. [CrossRef]
19. Michael, K.; Haug, K. Hydrodynamic trapping of injected acid gas in the Alberta Basin, Western Canada. In Proceedings of the 7th International Conference on Greenhouse Gas Control Technologies, Vancouver, BC, Canada, 5 September 2005.
20. Wang, T.; Dou, W.T.; Liu, X. The origin of formation water and the regularity of gas and water distribution for the Sulige gas field, Ordos Basin. *Acta Petrol. Sin.* **2010**, *5*, 13.
21. Wei, Y.S.W.; Shao, H.; Jia, A.L.; He, D.B.; Ji, L.D.; Fan, R. Gas water distribution model and control factors in low permeability high water saturation sandstone gas reservoirs. *Nat. Gas Geosci.* **2009**, *20*, 822–826.
22. Chen, D.; Wang, L.; Pang, X.; Bai, T. Geological characteristics and hydrocarbon accumulation models of the tight-sand gas reservoirs in upper Triassic Xujiahe Formation in Western Sichuan depression of China. In Proceedings of the Unconventional Resources Technology Conference, Colorado, Denver, USA, 12–14 August 2013.
23. Liu, G.D.; Sun, M.L.; Zhao, Z.Y.; Wang, X.B.; Wu, S.H. Characteristics and accumulation mechanism of tight sandstone gas reservoirs in the Upper Paleozoic, northern Ordos Basin, China. *Petrol. Sci.* **2013**, *10*, 442–449. [CrossRef]
24. Mann, U.; Hantschel, T.; Schaefer, R.; Krooss, B.; Leythaeuser, D.; Littke, R.; Sachsenhofer, R. Petroleum migration: Mechanisms, pathways, efficiencies and numerical simulations. In *Petroleum and Basin Evolution*; Welte, D.H., Horsfield, B., Baker, D.R., Eds.; Springer: Berlin/Heidelberg, Germany, 1997; pp. 403–520.
25. Zeng, J.H.; Yang, Z.F.; Feng, X.; Qiao, J.C.; Zhang, Z.Y. Study status and key scientific issue of tight reservoir oil and gas accumulation mechanism. *Adv. Earth Sci.* **2014**, *29*, 651–661.
26. Zou, C.; Tao, S.; Zhang, X.; He, D.; Zhou, C.; Gao, X. Geologic characteristics, controlling factors and hydrocarbon accumulation mechanisms of China's Large Gas Provinces of low porosity and permeability. *Sci. China Ser. D Earth Sci.* **2009**, *52*, 1068–1090. [CrossRef]
27. Barker, C. Aquathermal pressuring–Role of temperature in development of abnormal-pressure zones. *AAPG Bull.* **1972**, *56*, 2068–2071.
28. Li, M.; Li, J. Dynamic trap: A main action of hydrocarbon charging to form accumulations in low permeability-tight reservoir. *Acta Petrol. Sin.* **2010**, *31*, 718–722.
29. Spencer, C.W. Hydrocarbon generation as a mechanism for overpressuring in Rocky Mountain region. *AAPG Bull.* **1987**, *71*, 368–388.
30. Swarbrick, R. Reservoir diagenesis and hydrocarbon migration under hydrostatic palaeopressure conditions. *Clay Miner.* **1994**, *29*, 473–474. [CrossRef]
31. Wang, X.M.; Zhao, J.Z.; Liu, X.S. Occurrence state and production mechanism of formation water in tight sandstone reservoirs of Sulige area, Ordos Basin. *Petrol. Geol. Exp.* **2012**, *34*, 400–405.
32. Yang, F.; Ming, Z.; Jiang, L. Charging mechanism of tight sandstone gas reservoir and its pattern of accumulation and enrichment. *Fault Block Oil Gas Field* **2014**, *21*, 1–6.
33. Amann-Hildenbrand, A.; Ghanizadeh, A.; Krooss, B.M. Transport properties of unconventional gas systems. *Mar. Petrol. Geol.* **2012**, *31*, 90–99. [CrossRef]

34. Sakhaee-Pour, A.; Bryant, S.L. Effect of pore structure on the producibility of tight-gas sandstones. *AAPG Bull.* **2014**, *98*, 663–694. [CrossRef]
35. Zeng, J.; Feng, X.; Feng, S.; Zhang, Y.; Qiao, J.; Yang, Z. Influence of tight sandstone micro-nano pore-throat structures on petroleum accumulation: Evidence from experimental simulation combining X-ray tomography. *J. Nanosci. Nanotechnol.* **2017**, *17*, 6459–6469. [CrossRef]
36. Clarkson, C.R.; Solano, N.; Bustin, R.M.; Bustin, A.M.M.; Chalmers, G.R.L.; He, L.L.; Melnichenko, Y.B.; Radliński, A.P.; Blach, T.P. Pore structure characterization of North American shale gas reservoirs using USANS/SANS, gas adsorption, and mercury intrusion. *Fuel* **2013**, *103*, 606–616. [CrossRef]
37. Loucks, R.G.; Reed, R.M.; Ruppel, S.C.; Jarvie, D.M. Morphology, genesis, and distribution of nanometer-scale pores in siliceous mudstones of the Mississippian Barnett Shale. *J. Sediment. Res.* **2009**, *79*, 848–861. [CrossRef]
38. Nelson, P.H. Pore-throat sizes in sandstones, tight sandstones, and shales. *AAPG Bull.* **2009**, *93*, 329–340. [CrossRef]
39. Clarkson, C.R.; Wood, J.; Burgis, S.; Aquino, S.; Freeman, M. Nanopore-structure analysis and permeability predictions for a tight gas siltstone reservoir by use of low-pressure adsorption and mercury-intrusion techniques. *SPE Reserv. Eval. Eng.* **2012**, *15*, 648–661. [CrossRef]
40. Schmitt, M.; Fernandes, C.P.; da Cunha Neto, J.A.; Wolf, F.G.; dos Santos, V.S. Characterization of pore systems in seal rocks using nitrogen gas adsorption combined with mercury injection capillary pressure techniques. *Mar. Petrol. Geol.* **2013**, *39*, 138–149. [CrossRef]
41. Xiao, D.; Lu, Z.; Jiang, S.; Lu, S. Comparison and integration of experimental methods to characterize the full-range pore features of tight gas sandstone—A case study in Songliao Basin of China. *J. Nat. Gas Sci. Eng.* **2016**, *34*, 1412–1421. [CrossRef]
42. Cooper, J.; Wang, X.; Mohanty, K. Non-Darcy-flow studies in anisotropic porous media. *SPE J.* **1999**, *4*, 334–341. [CrossRef]
43. Freeman, C.; Moridis, G.; Blasingame, T. A numerical study of microscale flow behavior in tight gas and shale gas reservoir systems. *Transp. Porous Media* **2011**, *90*, 253. [CrossRef]
44. Khlaifat, A.L.; Arastoopour, H.; Qutob, H. Non-Darcy Flow in Tight Gas Reservoir of Travis Peak Formation. In Proceedings of the SPE Middle East Unconventional Gas Conference and Exhibition, Muscat, Omen, 31 January–2 February 2011.
45. Noman, R.; Archer, J. The effect of pore structure on non-Darcy gas flow in some low-permeability reservoir rocks. In Proceedings of the Low Permeability Reservoirs Symposium, Denver, CO, USA, 18–19 May 1987.
46. Raoof, A.; Hassanizadeh, S. A new formulation for pore-network modeling of two-phase flow. *Water Resour. Res.* **2012**, *48*, W01514. [CrossRef]
47. Zeng, J.; Zhang, Y.; Zhang, S.; Qiao, J.; Feng, X.; Feng, S. Experimental and theoretical characterization of the natural gas migration and accumulation mechanism in low-permeability (tight) sandstone cores. *J. Natl. Gas Sci. Eng.* **2016**, *33*, 1308–1315. [CrossRef]
48. Ghanizadeh, A.; Clarkson, C.R.; Aquino, S.; Ardakani, O.H.; Sanei, H. Petrophysical and geomechanical characteristics of Canadian tight oil and liquid-rich gas reservoirs: I. Pore network and permeability characterization. *Fuel* **2015**, *153*, 664–681. [CrossRef]
49. Schrama, E.; Naughton-Rumbo, R.; van der Bas, F.; Norris, M.R.; Shaoul, J.R. First true tight gas (<0.1 mD) horizontal multiple fracture well in the North Sea. In Proceedings of the SPE European Formation Damage Conference, Noordwijk, The Netherlands, 7–10 June 2011.
50. Stroker, T.M.; Harris, N.B.; Elliott, W.C.; Wampler, J.M. Diagenesis of a tight gas sand reservoir: Upper Cretaceous Mesaverde Group, Piceance Basin, Colorado. *Mar. Petrol. Geol.* **2013**, *40*, 48–68. [CrossRef]
51. Tobin, R.C.; McClain, T.; Lieber, R.B.; Ozkan, A.; Banfield, L.A.; Marchand, A.M.; McRae, L.E. Reservoir quality modeling of tight-gas sands in Wamsutter field: Integration of diagenesis, petroleum systems, and production data. *AAPG Bull.* **2010**, *94*, 1229–1266. [CrossRef]
52. Wescott, W.A. Diagenesis of Cotton Valley sandstone (Upper Jurassic), East Texas: Implications for tight gas formation pay recognition. *AAPG Bull.* **1983**, *67*, 1002–1013.
53. Qiao, J.C.; Zeng, J.H.; Feng, X.; Yang, Z.F.; Zhang, Y.C.; Feng, S. Characteristics of nano-nicro pore networks and petroleum microscopic occurrence state in ultra-low permeability (tight) sandstone reservoir. *J. Nanosci. Nanotechnol.* **2017**, *17*, 6039–6050. [CrossRef]

54. Zhao, H.W.; Ning, Z.F.; Wang, Q.; Zhang, R.; Zhao, T.Y.; Niu, T.F.; Zeng, Y. Petrophysical characterization of tight oil reservoirs using pressure-controlled porosimetry combined with rate-controlled porosimetry. *Fuel* **2015**, *154*, 233–242. [CrossRef]
55. Yang, H.; Fu, J.; Liu, X.; Meng, P. Accumulation conditions and exploration and development of tight gas in the Upper Paleozoic of the Ordos Basin. *Petrol. Explor. Dev.* **2012**, *39*, 315–324. [CrossRef]
56. Zhang, S.C.; Mi, J.K.; Liu, L.H.; Tao, S.Z. Geological features and formation of coal-formed tight sandstone gas pools in China: Cases from Upper Paleozoic gas pools, Ordos Basin and Xujiahe Formation gas pools, Sichuan Basin. *Petrol. Explor. Dev.* **2009**, *36*, 320–330.
57. Xiao, X.; Zhao, B.; Thu, Z.; Song, Z.; Wilkins, R. Upper Paleozoic petroleum system, Ordos Basin, China. *Mar. Petrol. Geol.* **2005**, *22*, 945–963. [CrossRef]
58. Tang, H.F.; Peng, S.M.; Zhao, Y.C. Characteristics of pore structure and reservoir evaluation in H2+3 Tight gas reservoir, Daniudi Gas Field. *J. Miner. Petrol.* **2006**, *26*, 107–113.
59. Luo, D.; Chen, S.; Zhang, G. New understandings of the Upper Paleozoic sedimentary facies and gas accumulation patterns in Daniudi gas field. *Oil Gas Geol.* **2011**, *32*, 368–374.
60. You, H.; Zhao, J.; Chen, H. Depositional characteristic and depositional model of Shanxi Formation to Xiashihezi Formation in the Daniudi gas field, Ordos Basin, China. *J. Chengdu Univ. Technol.* **2007**, *34*, 401.
61. Yuan, J.; Liu, G.D. Distribution characteristics and formation process of Upper Paleozoic abnormally low pressure zones in Ordos basin. *Oil Gas Geol.* **2005**, *26*, 792–799.
62. Liu, Q.; Jin, Z.; Meng, Q.; Wu, X.; Jia, H. Genetic types of natural gas and filling patterns in Daniudi gas field, Ordos Basin, China. *J. Asian Earth Sci.* **2015**, *107*, 1–11. [CrossRef]
63. Hao, S.M.; Li, L.; You, H.Z. Permo-Carboniferous paralic depositional systems in the Daniudi gas field and its near-source box-type gas accumulation-forming model. *Geol. China* **2007**, *4*, 9.
64. Wu, H.; Ji, Y.L.; Liu, R.; Zhang, C.L.; Chen, S. Insight into the Pore Structure of Tight Gas Sandstones: A Case Study in the Ordos Basin, NW China. *Energy Fuels* **2017**, *31*, 13159–13178. [CrossRef]
65. Blunt, M.J.; Bijeljic, B.; Dong, H.; Gharbi, O.; Iglauer, S.; Mostaghimi, P.; Paluszny, A.; Pentland, C. Pore-scale imaging and modelling. *Adv. Water Resour.* **2013**, *51*, 197–216. [CrossRef]
66. Valvatne, P.H.; Blunt, M.J. Predictive pore-scale network modeling. In Proceedings of the SPE Annual Technical Conference and Exhibition, Denver, CO, USA, 5–8 October 2003.
67. Wildenschild, D.; Sheppard, A.P. X-ray imaging and analysis techniques for quantifying pore-scale structure and processes in subsurface porous medium systems. *Adv. Water Resour.* **2013**, *51*, 217–246. [CrossRef]
68. Huang, Y. Nonlinear percolation feature in low permeability reservoir. *Spec. Oil Gas Reserv.* **1997**, *4*, 10–14.
69. Zhu, Z.; Zeng, J.; Wu, H.; Feng, Z.; Zhang, S.; Liang, X.; Sheng, X. An experimental study on oil migration and accumulation in low-permeability sandstone. *Oil Gas Geol.* **2007**, *28*, 229–234.
70. Ren, X.; Yan, Q.; He, Q. The Experimental Study of Characteristics of Gas Flow in Tight Formation. *J. Xian Petrol. Inst.* **1997**, *3*, 22–25.
71. Lv, C.; Wang, J.; Sun, Z. An experimental study on starting pressure gradient of fluids flow in low permeability sandstone porous media. *Petrol. Explor. Dev.* **2002**, *29*, 86–89.
72. Rouquerol, J.; Avnir, D.; Fairbridge, C.W.; Everett, D.H.; Haynes, J.M.; Pernicone, N.; Ramsay, J.D.F.; Sing, K.S.W.; Unger, K.K. Recommendations for the characterization of porous solids (Technical Report). *Pure Appl. Chem.* **1994**, *66*, 1739. [CrossRef]
73. Loucks, R.G.; Reed, R.M.; Ruppel, S.C.; Hammes, U. Spectrum of pore types and networks in mudrocks and a descriptive classification for matrix-related mudrock pores. *AAPG Bull.* **2012**, *96*, 1071–1098. [CrossRef]
74. Zeng, J.; Cheng, S.; Kong, X.; Guo, K.; Wang, H. Non-Darcy flow in oil accumulation (oil displacing water) and relative permeability and oil saturation characteristics of low-permeability sandstones. *Petrol. Sci.* **2010**, *7*, 20–30. [CrossRef]
75. Zheng, M.; Li, J.Z.; Wu, X.Z.; Li, P.; Wang, W.G.; Wang, S.J.; Xie, H.B. Physical modeling of oil charging in tight reservoirs: A case study of Permian Lucaogou Formation in Jimsar Sag, Junggar Basin, NW China. *Petrol. Explor. Dev.* **2016**, *43*, 241–250. [CrossRef]
76. Aguilera, R. Flow units: From conventional to tight gas to shale gas reservoirs. In Proceedings of the Trinidad and Tobago Energy Resources Conference, Port of Spain, Trinidad, 27–30 June 2010.
77. Clarkson, C.R.; Jensen, J.L.; Pedersen, P.K.; Freeman, M. Innovative methods for flow-unit and pore-structure analyses in a tight siltstone and shale gas reservoir. *AAPG Bull.* **2012**, *96*, 355–374. [CrossRef]

78. Dullien, F.A. *Porous Media: Fluid Transport and Pore Structure*; Academic press: San Diego, CA, USA, 2012.
79. Washburn, E.W. The dynamics of capillary flow. *Phys. Rev.* **1921**, *17*, 273. [CrossRef]